# Permeance-harmonic-oriented Design and Optimization of a Field-modulated PM Hub Motor for High Torque Density

Yuting Zhou, Zixuan Xiang, Xiaoyong Zhu, *Member*, *IEEE*, Qian Liu, Deyang Fan, *Member*, *IEEE*, and Kunhua Chen

***Abstract*—This paper investigates an aggregated design and optimization method for permanent magnet hub (PMH) motors, guided by permeance harmonics, to meet low-speed, high-torque requirements. The key lies in establishing the correlation between stator and rotor permeance harmonics and torque. Firstly, contribution equations describing the influence of stator and rotor permeance harmonics on torque are derived. It reveals that the contribution degree is affected by harmonic amplitude and phase. Then, the selection criteria for stator and rotor topology are formulated. The amplitude and phase characteristics of the permeance harmonic group are considered in criteria, which aim to achieve the aggregated design from a permeance harmonic perspective. Furthermore, based on the identified aggregated permeance harmonics, the airgap flux density harmonics directly linked to permeance harmonics are determined. Taking these harmonics as the goal, they are involved in the optimization process for high torque density. Sensitivity analysis and response surface analysis are adopted, respectively, to lock the design variables and their parameter ranges. Then, the motor topology with characteristics of high torque density is obtained through multi-objective optimization. Finally, a prototype experiment is conducted on the optimized PMH motor..**

***Index Terms*—Permanent magnet hub (PMH) motor, torque density, harmonic characteristic.**

## I. INTRODUCTION

IN distributed drive systems for electric vehicles (EVs), permanent magnet hub (PMH) motors are highly favored due to their high level of integration [1]-[2]. However, this application scenario imposes extremely stringent requirements on the motor, that is, providing high torque at low speeds to meet demands, while simultaneously maintaining strict weight control to improve energy efficiency [3]-[4]. Among various candidate motor types, the field-modulated motor (FMM) is regarded as a highly promising solution due to its simple structure and high torque density [5]-[6]. Compared to traditional permanent magnet (PM) synchronous machines, the FMM can generate higher torque output through magnetic field modulation effects, making it particularly suitable for in-wheel drive applications where space and weight are critical concerns [7]-[8].

To fully exploit the torque potential of FMMs, existing research primarily progresses from the design and optimization of the excitation source and modulator. On one hand, related studies focus on innovations in PM topology aimed at enhancing the PM magnetomotive force (PM MMF) [9]-[10]. Researchers have proposed various PM arrangements, such as surface-mounted [11], spoke-type [12], V-shaped [13], and double-sided PM configurations [14]-[15]. Building upon these PM topologies, further optimizations involving shape design [16], and special arrays like segmented and staggered trapezoidal poles [17], Halbach arrays [18] have been implemented. These refinements effectively improve the torque by improving PM MMF.

In addition, the modulator constitutes another critical factor affecting the modulation performance [19]-[20]. In [21], it is found that key dimensional parameters of the stator modulator, such as the pole arc and tooth width, are directly related to the harmonic amplitudes of the airgap magnetic field, which consequently affects motor performance metrics. Moreover, methods such as employing notches [22] and specific shaping designs to improve the fundamental-to-harmonic ratio can, to some extent, achieve a reduction in motor torque ripple [23]-[24]. Consequently, optimizing the modulator has proven to be an effective pathway for improving performance, gradually leading to a series of targeted design methodologies that use modulator permeance as a bridge [25]-[27]. Specifically, by establishing the relationship between stator dimensional parameters and the stator permeance function, research pathways that utilize stator permeance harmonics as a medium for enhancing motor torque performance have been developed [28]-[30]. In [31], a coded-tooth stator is proposed, enabling multi-degree-of-freedom oriented design of stator permeance harmonics. Consequently, irregular airgap topologies provide a feasible

Manuscript received February 01, 2026; revised April 13, 2026 and May 13, 2026; accepted May 18, 2026. Date of publication June 25, 2026. Date of current version June 9, 2026.

This work was supported by the National Natural Science Foundation of China under Grant 52577056.

Yuting Zhou, Zixuan Xiang, Xiaoyong Zhu, Deyang Fan, and Kunhua Chen are with the School of Electrical and Information Engineering, Jiangsu University, Zhenjiang 212013, China (e-mail: 2112407126@stmail.ujs.edu.cn; zxxiang@ujs.edu.cn; zxyff@ujs.edu.cn; Deyang.Fan@ujs.edu.cn; chenkunhua@itjiyi.com).

Qian Liu is with the School of Physics and Electronic Engineering, Jiangsu University, Zhenjiang 212013, China (e-mail: lqxyd@ujs.edu.cn).

(Corresponding author: *Zixuan Xiang*)

Digital Object Identifier 10.30941/CESTEMS.2026.00020.

pathway for improving the distribution of airgap harmonics, thereby enhancing torque and reducing ripple.

It is worth noting that research on coded-tooth structures has predominantly been applied to surface-mounted PM topologies [32]-[33]. For other motor configurations, such as spoke-type or V-shaped PM structures, the rotor structure influences the fundamental and harmonic components of the PM MMF, manifesting as a synchronous modulation of the harmonic amplitudes [34]. This has consequently drawn research attention to the modulation effects of rotor permeance harmonics [35]-[36]. In [36], by adopting a rotor T-shaped notch design, the effects of different notch positions on optimizing the waveform of the airgap flux density and improving torque performance are discussed, which is considered to alter the rotor permeance harmonics to some extent. In [37], the modulation effect of rotor salient-pole reluctance is analyzed, clarifying the prominent role of the 0th, 1st, and 2nd-order rotor permeance harmonics in the airgap magnetic field. In summary, most current research focuses on the modulation principles and design of unilateral permeance, lacking a comprehensive consideration of permeance harmonics from both sides. Therefore, this paper approaches the design from the perspective of the integrated regulation of stator and rotor permeance harmonics, aiming to fully utilize the amplitude and phase characteristics of these harmonics to maximize positive torque contribution.

This paper introduces a motor aggregation design based on stator and rotor permeance harmonics and proposes a multi-objective optimization method to realize the requirement of high torque at low speeds within a lower weight. The contributions of this paper can be summarized as follows: 1) The correlation model between permeance harmonics and torque is established, and a torque contribution factor is defined to screen key harmonics. 2) The stator and rotor topology selection criteria are proposed based on the amplitude and phase of aggregated permeance harmonics to maximize positive torque contribution. 3) The multi-objective optimization is implemented targeting key airgap flux density harmonics and a lightweight factor, enhancing torque density. Section II provides a theoretical analysis of the torque generation mechanism from the permeance harmonic perspective, defining and analyzing a torque contribution factor for permeance harmonics. Section III builds topology selection criteria leveraging the amplitude and phase characteristics of permeance harmonics related to torque. It then investigates and compares specific stator and rotor permeance topologies, analyzing the resulting permeance harmonic distributions. In Section IV, to address lightweight design requirements, multi-objective optimization is formulated considering both a lightweight factor and flux harmonic content. Parameter sensitivity screening and response surface methodology are employed to constrain design variables and their ranges. In addition, performance analysis and evaluation are conducted in motors before and after the design of magnetic conduction harmonics, as well as the optimal motor. Finally, Section V presents experimental validation of the proposed motor.

## II. Concept of Permeance-harmonic-oriented Aggregated Design and Theoretical Analysis

### *A. Method of Permeance-harmonic-oriented Aggregated Design and Optimization*

To achieve high torque density, a design method from permeance-harmonic-oriented perspective is shown in Fig. 1. Based on field modulation principle, the abundant air gap harmonics of flux-modulated PM hub (FMPMH) motor come from key elements, including the magnetic source, the stator and rotor permeance, etc. Among them, the stator and rotor permeance can be decomposed into harmonics with different amplitudes and phases, and then the correlation relationship between airgap permeance harmonics and the torque can be determined. Based on it, the comparison and design of motor topology elements can be carried out respectively, considering the torque transmission capability and aggregation characteristics of stator and rotor permeance harmonics. Furthermore, the airgap flux density harmonics generated by the permeance harmonics that make a stable positive contribution to the torque can be clearly identified. Combined with the design requirements of high torque density and light weight of hub motors, the light weight factor is defined and, together with flux density harmonics, is taken as an objective to optimize. During the process, sensitivity analysis and response surface analysis are adopted, respectively, to lock the highly sensitive parameters and their ranges, thereby effectively determining the final topology.

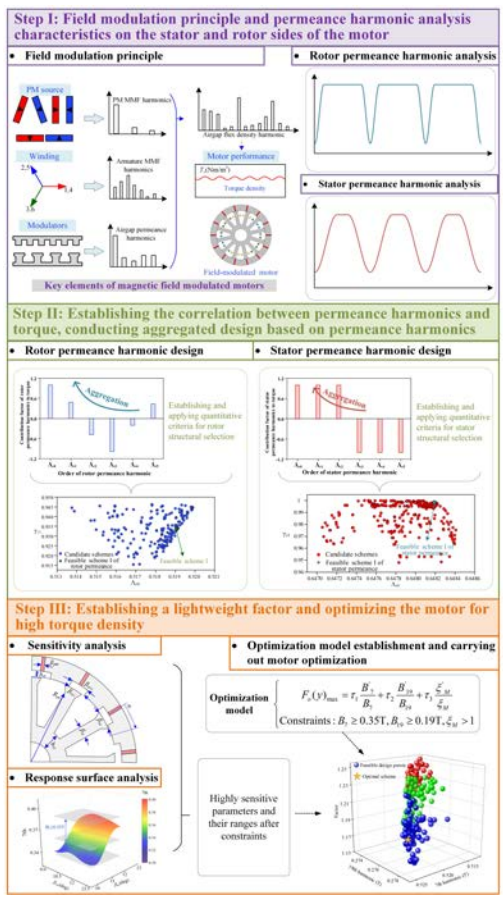


Fig. 1. The concept of permeance-harmonic-oriented design and optimization.

### B. Theoretical Analysis

In this part, the influence of permeance harmonics on motor torque is derived and analyzed, providing a theoretical basis for the subsequent motor topology design.

The PM MMF of the motor can be expressed as [27]:

$$F_{\mathrm{pm}}(\theta,t)=\sum_{i=1,3,5\cdots}^{+\infty}F_{\mathrm{pm}i}\cos\left[iP_{\mathrm{r}}(\theta-\omega_{\mathrm{r}}t)\right] \tag{1}$$

where $F_{\mathrm{pm}i}$ represents the amplitude of the $i$-th MMF harmonic, $\omega_{\mathrm{r}}$ is the mechanical speed of the motor, and $P_{\mathrm{r}}$ is the pole-pair number. $\theta$ represents the airgap circumferential position angle and $t$ represents a specific moment during the operation of the motor.

The synchronous modulation effect on the rotor side is derived, and the no-load airgap magnetic flux density of the motor can be expressed as:

$$\begin{aligned}&B_{\mathrm{g\_Rotor}}(\theta,t)=F_{\mathrm{pm}}(\theta,t)\cdot\Lambda_{\mathrm{r}}(\theta,t)\cdot\Lambda_{\mathrm{s}}\\&=\Lambda_{\mathrm{s}}\Lambda_{\mathrm{r0}}\sum_{i=1,3,5\cdots}^{+\infty}F_{\mathrm{pm}i}\cos\left[iP_{\mathrm{r}}(\theta+\omega_{\mathrm{r}}t+\theta_0)\right]\\&+\frac{1}{2}\Lambda_{\mathrm{s}}\sum_{i=1,3,5\cdots}^{+\infty}\sum_{n}^{+\infty}F_{\mathrm{pm}i}\Lambda_{rn}\left\{\cos\left[\left(iP_{\mathrm{r}}\pm nN_{\mathrm{rt}}\right)(\theta+\omega_{\mathrm{r}}t)+iP_{\mathrm{r}}\theta_0\pm\theta_{rn}\right]\right\}\end{aligned} \tag{2}$$

where $\theta_0$ is the initial position, $\Lambda_{\mathrm{r}}$ and $\Lambda_{\mathrm{s}}$ are the rotor and stator permeance. $\Lambda_{rn}$ and $\theta_{rn}$ are the amplitude and phase of $n$-th rotor permeance harmonic, respectively. $\Lambda_{\mathrm{r0}}$ is the direct current (DC) component of rotor permeance. $N_{\mathrm{rt}}$ is the number of the rotor poles.

According to [28], the output torque in FMMs is mostly generated by the fundamental harmonic of PM MMF. Therefore, $i$ is taken as 1. And on the premise that only the modulation effect of the rotor permeance is considered, no-load airgap flux density can be simplified as:

$$\begin{aligned}&B_{\mathrm{g\_Rotor}}(\theta,t)=\Lambda_{\mathrm{r0}}\Lambda_{\mathrm{s}}F_{\mathrm{pm1}}\cos\left[P_{\mathrm{r}}(\theta+\omega_{\mathrm{r}}t+\theta_0)\right]\\&+\frac{1}{2}\Lambda_{\mathrm{s}}F_{\mathrm{pm1}}\sum_{n}^{+\infty}\Lambda_{rn}\left\{\cos\left[\left(P_{\mathrm{r}}\pm nN_{\mathrm{rt}}\right)(\theta+\omega_{\mathrm{r}}t)+P_{\mathrm{r}}\theta_0\pm\theta_{rn}\right]\right\}\end{aligned} \tag{3}$$

Next, PM flux linkage $\psi_{\mathrm{ph}}$ can be obtained by integrating the no-load airgap magnetic flux density and expressed as:

$$\Psi_{\mathrm{ph}}(t)=C\int_0^{\frac{2\pi}{N_{\mathrm{st}}}}B_{\mathrm{g\_Rotor}}(\theta,t)\,\mathrm{d}\theta \tag{4}$$

where the constant $C = k_{\mathrm{d1}}N_{\mathrm{ph}}L_{\mathrm{ef}}R_{\mathrm{g}}$, $k_{\mathrm{d1}}$ is the winding distribution coefficient of the fundamental harmonic, $N_{\mathrm{ph}}$, $L_{\mathrm{ef}}$, and $R_{\mathrm{g}}$ are, respectively, winding turns, axis length, and airgap radius of the motor. $N_{\mathrm{st}}$ is the number of the stator teeth.

After further derivation, the back electromotive force (EMF) can be calculated as:

$$\begin{aligned}&e_{\mathrm{ph}}(t)=-\frac{\mathrm{d}\Psi_{\mathrm{ph}}(t)}{\mathrm{d}t}\\&=C\omega_{\mathrm{r}}F_{\mathrm{pm1}}\Lambda_{\mathrm{r0}}\left\{\cos\left[P_{\mathrm{r}}\left(\frac{2\pi}{N_{\mathrm{st}}}+\omega_{\mathrm{r}}t\right)\right]-\cos\left(P_{\mathrm{r}}\omega_{\mathrm{r}}t\right)\right\}\\&+\frac{C}{2}\omega_{\mathrm{r}}F_{\mathrm{pm1}}\sum_{n}\Lambda_{rn}\cos\left(\theta_{rn}\right)\\&\left\{\cos\left[\left(P_{\mathrm{r}}\pm nN_{\mathrm{rt}}\right)\left(\frac{2\pi}{N_{\mathrm{st}}}+\omega_{\mathrm{r}}t\right)\right]-\cos\left(P_{\mathrm{r}}\pm nN_{\mathrm{rt}}\right)\omega_{\mathrm{r}}t\right\}\end{aligned} \tag{5}$$

According to the above equation, the amplitude of back EMF $E_{\mathrm{ph}}$ can be expressed as:

$$\begin{aligned}&E_{\mathrm{ph}}=C\omega_{\mathrm{r}}\Lambda_{\mathrm{r0}}F_{\mathrm{pm1}}\cos\left(2\pi\frac{P_{\mathrm{r}}}{N_{\mathrm{st}}}\right)\\&+\frac{C}{2}\omega_{\mathrm{r}}F_{\mathrm{pm1}}\sum_{n}\Lambda_{rn}\cos\left(\theta_{rn}\right)\cos\left(2\pi\frac{P_{\mathrm{r}}\pm nN_{\mathrm{rt}}}{N_{\mathrm{st}}}\right)\end{aligned} \tag{6}$$

When the motor adopts the brushless alternating current (AC) control mode with d-axis current $i_{\mathrm{d}} = 0$, the electromagnetic torque can be expressed as:

$$\begin{aligned}&T_{\mathrm{eR}}=\frac{mE_{\mathrm{ph}}I_{\mathrm{ph}}}{2\omega_r}=\frac{mI_{\mathrm{ph}}CF_{\mathrm{pm1}}}{2}\cos\left(\frac{2\pi P_{\mathrm{r}}}{N_{\mathrm{st}}}\right)\Lambda_{\mathrm{r0}}\\&+\frac{mI_{\mathrm{ph}}CF_{\mathrm{pm1}}}{4}\cos\left[\frac{2\pi\left(P_{\mathrm{r}}\pm nN_{\mathrm{rt}}\right)}{N_{\mathrm{st}}}\right]\sum_{n}\Lambda_{rn}\cos\left(\theta_{rn}\right)\end{aligned} \tag{7}$$

where $m$ is the number of motor phases and $I_{\mathrm{ph}}$ represents the amplitude of the input current. Torque under the modulation effect of only stator permeance can be calculated as:

$$\begin{aligned}&T_{\mathrm{eS}}=\frac{mE_{\mathrm{ph}}I_{\mathrm{ph}}}{2\omega_r}=\frac{mI_{\mathrm{ph}}CF_{\mathrm{pm1}}}{2}\cos\left(\frac{2\pi P_{\mathrm{r}}}{N_{\mathrm{st}}}\right)\Lambda_{\mathrm{s0}}\\&+\frac{mI_{\mathrm{ph}}CF_{\mathrm{pm1}}}{4}\cos\left[\frac{2\pi(P_{\mathrm{r}}\pm vN_{\mathrm{st}})}{N_{\mathrm{st}}}\right]\sum_{v}\Lambda_{\mathrm{sv}}\cos\left(\theta_{\mathrm{sv}}\right)\end{aligned} \tag{8}$$

where $\Lambda_{\mathrm{sv}}$ and $\theta_{\mathrm{sv}}$ are the amplitude and phase of $v$-th stator permeance harmonic, respectively. $\Lambda_{\mathrm{s0}}$ is the DC component of stator permeance. The contribution factor $\lambda$ of airgap permeance harmonics to the output torque is defined as:

$$\lambda_{rn}=\frac{T_n}{\Lambda_{rn}},\lambda_{\mathrm{sv}}=\frac{T_v}{\Lambda_{\mathrm{sv}}} \tag{9}$$

where $T_n$ and $T_v$ represent torque components generated by $n$-th rotor permeance harmonic and $v$-th stator permeance harmonic, respectively. Based on this, the influence of relevant permeance harmonics on the torque can be classified and calculated, as shown in Tables I and II. The average torque has two components. Under the same excitation source, the amplitude of the permeance harmonics directly determines torque. Meanwhile, the phase of the permeance harmonic determines whether its contribution to torque is positive or negative.

TABLE I
ROTOR PERMEANCE CONTRIBUTION TO TORQUE

| Harmonic order | Contribution factor, $\lambda$ | Phase of rotor permeance harmonics |
|---|---|---|
| 0 | $\frac{mI_{\mathrm{ph}}CF_{\mathrm{pm1}}}{2}\cos\left(\frac{2\pi P_{\mathrm{r}}}{N_{\mathrm{st}}}\right)$ | 0 |
| $n$ | $\frac{mI_{\mathrm{ph}}CF_{\mathrm{pm1}}}{4}\cos\left[\frac{2\pi\left(P_{\mathrm{r}}\pm nN_{\mathrm{rt}}\right)}{N_{\mathrm{st}}}\right]$ | $\theta_{rn}$ |

TABLE II
STATOR PERMEANCE CONTRIBUTION TO TORQUE

| Harmonic order | Contribution factor, $\lambda$ | Phase of stator permeance harmonics |
|---|---|---|
| 0 | $\frac{mI_{\mathrm{ph}}CF_{\mathrm{pm1}}}{2}\cos\left(\frac{2\pi P_{\mathrm{r}}}{N_{\mathrm{st}}}\right)$ | 0 |
| $v$ | $\frac{mI_{\mathrm{ph}}CF_{\mathrm{pm1}}}{4}\cos\left[\frac{2\pi\left(P_{\mathrm{r}}\pm vN_{\mathrm{st}}\right)}{N_{\mathrm{st}}}\right]$ | $\theta_{\mathrm{sv}}$ |

## III. Characteristic Analysis and Discussion of Permeance Harmonics

To meet the low-speed direct-drive requirements of hub motors, high torque density should be prioritized as the primary performance metric. This section establishes the relationship between permeance harmonics and torque. Subsequently, a topology optimization model centered on permeance harmonics for torque enhancement is developed, followed by a comparative analysis of the resulting permeance harmonic characteristics.

### *A. Analysis and Discussion of Rotor Permeance Harmonic*

Fig. 2 analyzes rotor permeance harmonics, with Figs. 2(a) and 2(b) depicting their amplitude and phase distributions. Figs. 2(c) present the resulting electromagnetic torque.

It reveals that the 0th rotor permeance harmonic exhibits both the highest amplitude and dominant torque contribution factor. Conversely, the 4th harmonic demonstrates minimal amplitude and negligible torque contribution. Notably, 2nd, 3rd, and 4th harmonics generate negative torque components due to negative values of their cosine phase. The 0th rotor permeance harmonic, maintains constant phase alignment and consistently contributes positive torque.

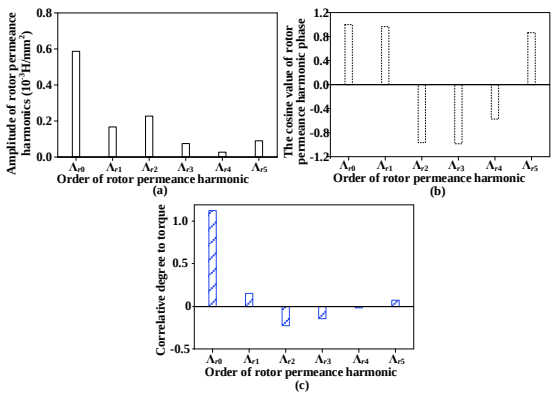


Fig. 2. The analysis of rotor airgap permeance. (a) Amplitude. (b) Phase cosine value. (c) Torque.

Based on the intrinsic characteristics of rotor permeance harmonics and their torque correlations, the following selection criteria are established. First, the 0th permeance harmonic exhibits the dominant amplitude and possesses a large torque contribution factor. Consequently, its amplitude serves as a primary design criterion. Simultaneously, to maximize positive torque contributions from higher-order rotor permeance harmonics, the sum of cosine phase values for harmonics with high contribution factors is defined as $\gamma_{r1}$. In addition, since the amplitudes of rotor permeance harmonics determine torque capacity, $\gamma_{r2}$ is defined as the cumulative amplitude of high-contribution harmonics. Based on the above, the quantitative criteria for structural selection are established:

$$\begin{cases} \text{Selection criterion 1}: F_{agg}(\Lambda r\_1) = k_1\Lambda_{r0} + k_2\gamma_{r1} \\ \text{Selection criterion 2}: F_{agg}(\Lambda r\_2) = k_1\Lambda_{r0} + k_2\gamma_{r2} \end{cases} \tag{10}$$

where $k_1$ and $k_2$ are weight coefficients. $\gamma_{r1}$ and $\gamma_{r2}$ are expressed as follows:

$$\begin{cases} \gamma_{r1} = \sum_{n=0(n\neq 4)}^{5} \cos(\theta_{rn}) \\ \gamma_{r2} = \sum_{n=0(n\neq 4)}^{5} \Lambda_{rn} \end{cases} \tag{11}$$

Fig. 3 presents the candidate schemes related to rotor permeance harmonics. Based on the selection criteria 1 in (10) for rotor permeance harmonics, feasible scheme 1 is determined. And, feasible scheme 2 is selected by selection criteria 2. Comparative analysis in Fig. 4 reveals significant permeance waveform modifications in Schemes I and II relative to the initial scheme, with Scheme II exhibiting higher amplitude. Next, increased amplitudes of 0th, 3rd, and 4th harmonics is beneficial to improve torque capacity, while phase polarity reversals occur in 3rd–4th harmonics of Scheme I and in 2nd–4th harmonics of Scheme II, signifying increased positive torque components as shown in Figs. 4(b) and 4(c). Further, Fig. 4(d) shows the torque comparison result of three schemes as presented in the per-unit form. Although residual negative torque contributions persist from the 2nd/5th harmonics of Scheme I and those from the 1st/5th harmonics of Scheme II, these are outweighed by combined torque polarity reversals in the harmonic. Ultimately, yielding total torque enhancement in the two schemes.

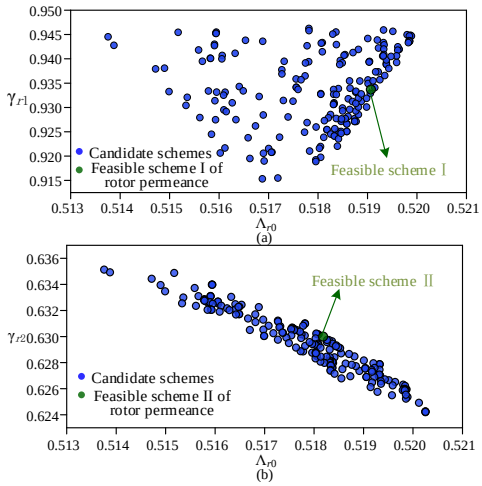


Fig. 3. Feasible design schemes of rotor airgap permeance. (a) Feasible scheme I. (b) Feasible scheme II.

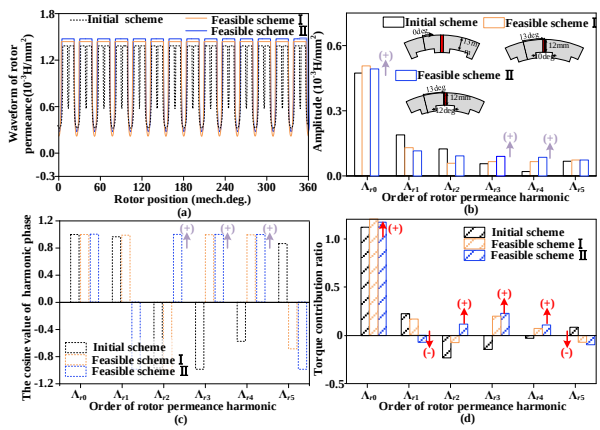


Fig. 4. Airgap permeance analysis of rotor modulators with different structures. (a) Waveform. (b) Amplitude. (c) Phase cosine value. (d) Torque.

Furthermore, as rotor permeance modulate the MMF, thereby affecting the harmonic composition of the airgap flux density, the airgap magnetic flux density and torque characteristics of the motor under the three rotor schemes are analyzed and presented in Fig. 5. It can be observed from Fig. 5(c) that the torque performance of Schemes I and II has improved, which corresponds to the change in the harmonic distribution and verifies the effectiveness of the rotor modulator selection principle to a certain extent.

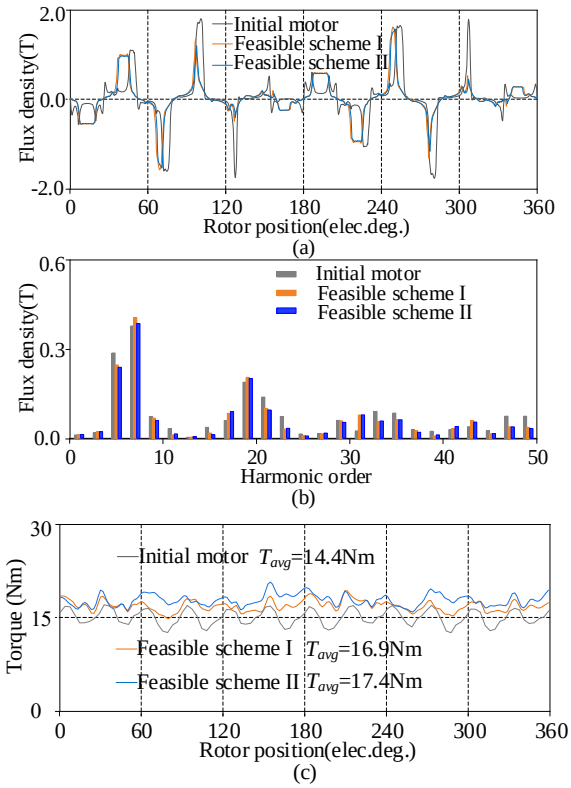


Fig. 5. Comparison and analysis of motor with different rotor structures. (a) Airgap flux density waveform. (b) Airgap flux density harmonic distribution. (c) Torque performance.

## B. *Analysis and Discussion of Stator Permeance Harmonic*

Fig. 6(a) reveals dominant amplitudes in the 0th and 1st stator permeance harmonics, indicating their greater influence on torque as shown in Fig. 6(c), whereas the 5th harmonic exhibits minimal torque contribution. Fig. 6(b) further demonstrates that torque component magnitudes scale with harmonic amplitudes across their orders, while positive or negative torque contribution is governed by its phase characteristics. In addition, Figs. 6(c) show different torque contribution factors across different stator permeance harmonics. Given its significant amplitude and consistent positive torque contribution as a DC component, the 0th harmonic amplitude constitutes a primary selection criterion. To maximize positive torque contributions from remaining harmonics, the sum of cosine phase values for harmonics is defined as $\gamma_{s1}$. The larger its value is, the more positive torque components generated. Simultaneously, $\gamma_{s2}$ is defined as the cumulative amplitude of high-contribution harmonics, with greater values indicating enhanced output capability.

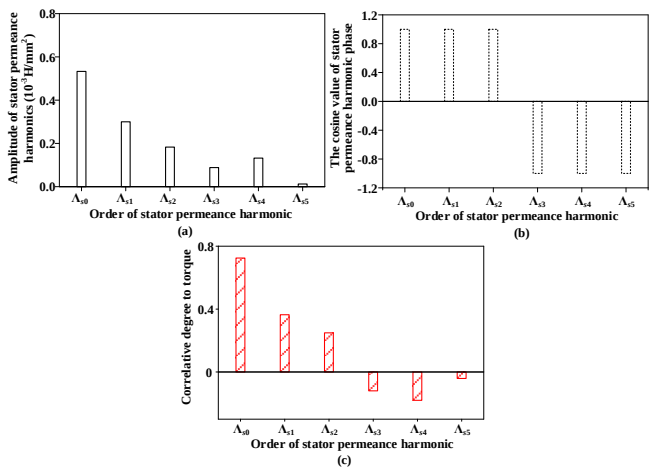


Fig. 6. The analysis of stator airgap permeance. (a) Amplitude. (b) Phase cosine value. (c) Torque contribution ratio.

Based on the above, the quantitative criteria for motor structural selection are established:

$$\begin{cases} \text{Selection criterion 1}: F_{\text{agg}}\left(\Lambda\text{s}\_1\right) = k_1\Lambda_{\text{s0}} + k_2\gamma_{\text{s1}} \\ \text{Selection criterion 2}: F_{\text{agg}}\left(\Lambda\text{s}\_2\right) = k_1\Lambda_{\text{s0}} + k_2\gamma_{\text{s2}} \end{cases} \tag{12}$$

where $\gamma_{\text{r1}}$ and $\gamma_{\text{r2}}$ are expressed as follows:

$$\begin{cases} \gamma_{\text{s1}} = \sum_{v=0}^{5} \cos\left(\theta_{sv}\right) \\ \gamma_{\text{s2}} = \sum_{v=0}^{5} \Lambda_{sv} \end{cases} \tag{13}$$

Through multi-objective genetic algorithm optimization incorporating airgap permeance harmonic selection criteria, Fig. 7 presents candidate schemes of stator permeance. The two feasible schemes are selected based on the value of the target function in (12).

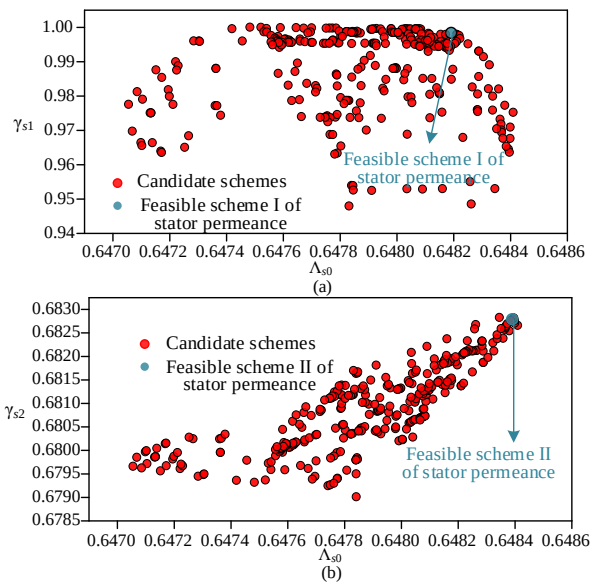


Fig. 7. Feasible design schemes of stator airgap permeance. (a) Feasible scheme I. (b) Feasible scheme II.

Fig. 8(b) demonstrates amplitude enhancement in the 0th, 1st, 2nd, and 5th harmonics for both feasible schemes I and II, while suppressing other harmonics. As evidenced in Fig. 8(d),

the amplified 0th harmonic significantly increases its torque contribution as presented in the per-unit form. Concurrently, phase modification in the 5th harmonic transforms its negative torque contribution into a positive one, as shown in Fig. 8(c), synergistically augmenting overall torque capacity.

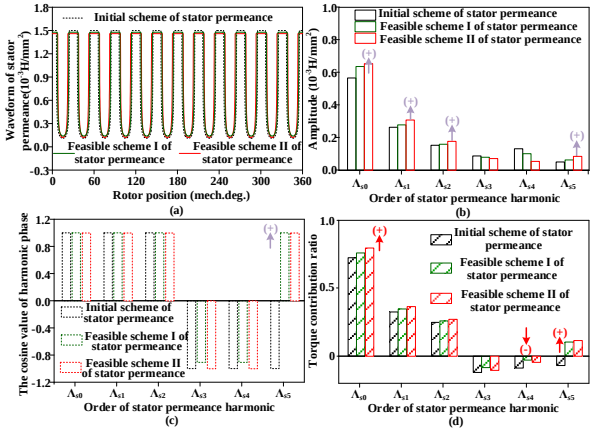


Fig. 8. Airgap permeance analysis of stator modulators with different structures. (a) Waveform. (b) Amplitude. (c) Phase cosine value. (d) Torque.

## IV. Optimization and Evaluation of Field-Modulated FMPMH Motor

This section investigates high-torque density and lightweight design optimization centered on these torque-critical flux density harmonics.

Building upon the permeance harmonic analysis of torque generation mechanisms in preceding sections, the 0th rotor and stator permeance harmonics emerge as dominant contributors to torque output, followed by 1st stator harmonic. The airgap harmonics associated with zero-order rotor permeance $\Lambda_{r0}$, zero-order stator permeance $\Lambda_{s0}$, and 1st-order stator permeance $\Lambda_{s1}$ are shown in Fig. 9(a), that is, 7th and 19th airgap flux density harmonics. This means that the 7th and 19th airgap harmonics demonstrate strong torque correlations, which is further verified in Fig. 9(b).

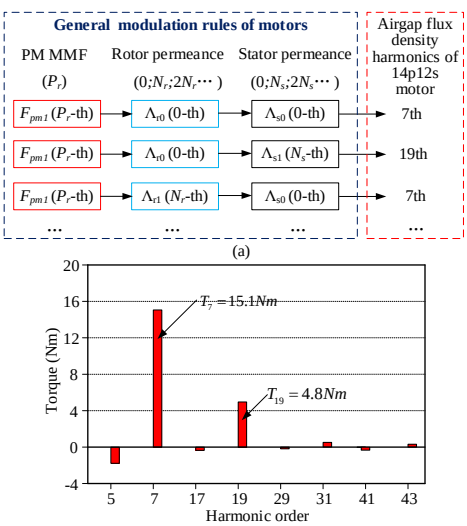


Fig. 9. (a) The modulation process of the PM field and the corresponding airgap flux density harmonics. (b) The torque generated by different airgap flux density harmonics of the proposed FMPMH motor.

### A. High-density Optimization

In the application of EVs, the design requirements for the motor are not only reflected in the high torque density, but also in the mass. Therefore, the light-weighting factor $\xi_M$ is defined in the form of the variation ratio of motor mass during the design process:

$$\xi_M = \frac{M_o}{M_p} \tag{14}$$

where $M_p$ denotes the mass of the motor during the design process, and $M_o$ represents the initial mass. Accounting for both torque density and mass imperatives, the motor optimization model is formulated with the constraint conditions specified in (15)

$$\begin{cases} F_{agg}(y)_{max} = \tau_1 \dfrac{B_7'}{B_7} + \tau_2 \dfrac{B_{19}'}{B_{19}} + \tau_3 \xi_M \\ \text{Constraints}: B_7 \geq 0.35\text{T}, B_{19} \geq 0.19\text{T}, \xi_M > 1 \end{cases} \tag{15}$$

where $\tau_1$, $\tau_2$, and $\tau_3$ denote the weighting coefficients for the 7th airgap harmonic, 19th airgap harmonic, and light-weighting factor, respectively. Prioritizing high-torque performance with consideration of the superior torque contribution of the 7th harmonic. Correspondingly, $B_7'$ and $B_{19}'$ represent the variational terms.

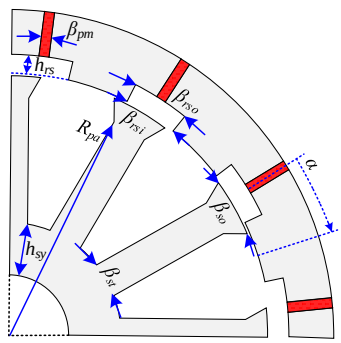


Fig. 10. Parametric model of the FMPMH motor.

TABLE III
Sensitivity Values of Design Parameters on Objective Performance

| Parameter variables | Optimization objective | | |
|---|---|---|---|
| | 7th harmonic | 19th harmonic | $\xi_M$ |
| $h_{sy}$ | 0.057701 | 0.090686 | 0.015537 |
| $\beta_{st}$ | 0.353343 | 0.479658 | 0.100192 |
| $\beta_{rsi}$ | 0.084345 | 0.104241 | 0.344492 |
| $h_{rs}$ | 0.33486 | 0.453654 | 0.857843 |
| $\beta_{rso}$ | 0.169533 | 0.134727 | 0.380273 |
| $\beta_{so}$ | 0.483545 | −0.13629 | 0.281296 |
| $R_{pa}$ | −0.14066 | 0.013547 | 0.011359 |
| $\alpha$ | 0.102681 | 0.166459 | 0.014864 |
| $\beta_{pm}$ | 0.013248 | 0.181798 | 0.188596 |

Fig. 10 presents the parametric motor model. Sensitivity analysis identifies design variables exhibiting significant influence on torque-related airgap flux density harmonics and the light-weighting factor, thereby streamlining the optimization workflow and enhancing computational efficiency.

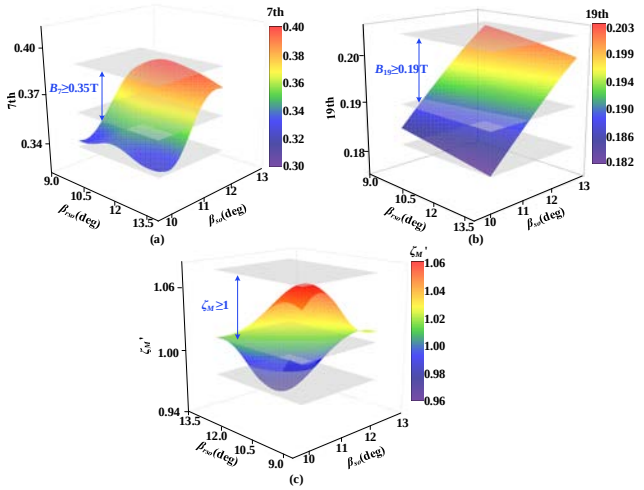


Fig. 11. The response surface analysis results of parameters $\beta_{rso}$ and $\beta_{so}$ on target performance. (a) 7th harmonic. (b) 19th harmonic. (c) $\zeta_M$.

Through the sensitivity analysis results in Table III, four design variables governing multi-objective optimization are selected for comprehensive response surface analysis. They are stator tooth angle $\beta_{st}$, rotor slot height $h_{rs}$, outer rotor slot width $\beta_{rso}$, and stator pole arc width $\beta_{so}$. Constraint-defined feasible subspaces within the response surface further narrow the design space, as shown in Figs. 11 and 12. Guided by hierarchical objectives prioritizing high torque density followed by mass reduction, parameter ranges optimizing both criteria are identified as detailed in Table IV.

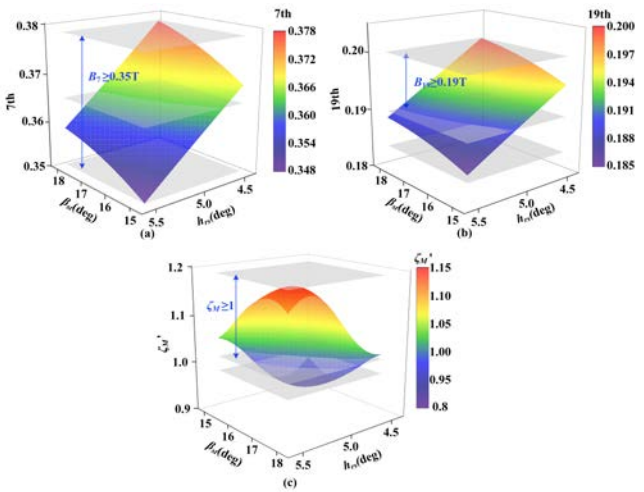


Fig. 12. The response surface analysis results of parameters $\beta_{st}$ and $h_{rs}$ on target performance. (a) 7th harmonic. (b) 19th harmonic. (c) $\xi_M$.

TABLE IV
THE INITIAL VALUE AND THE RANGE OF THE SELECTED PARAMETERS BASED ON RESPONSE SURFACE ANALYSIS

| Parameter variables | Initial value | Parameter range after constraints |
|---|---|---|
| $\beta_{rso}$/° | 12 | 10.6–14 |
| $\beta_{so}$/° | 12 | 11–14.5 |
| $\beta_{st}$/° | 17.6 | 16.8–18.5 |
| $h_{rs}$/mm | 5 | 4.5–5.2 |

The distribution of solutions obtained through multi-objective optimization is shown in Fig. 13. Fig. 13 illustrates the trade-off relationship between the 7th and 19th flux density harmonics and the lightweight coefficient. To better represent the differences among the design schemes, they are divided into three categories. Among them, the red and green feasible points achieve an excellent lightweight performance, but their weakened harmonic amplitudes affect the torque capacity. In contrast, the blue points are feasible design points that meet the optimization objective function (15). Subsequently, within the optimization framework, the final motor scheme is determined by balancing the torque density and reduction requirements.

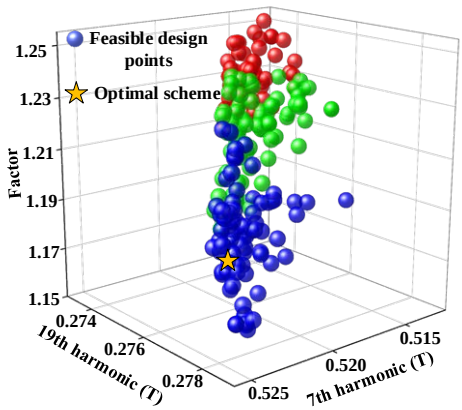


Fig. 13. The result of motor multi-objective optimization.

## B. *Performance Evaluation*

Electromagnetic performances of three topologies are comparatively analyzed, namely the motor before the modulator design, that after the modulator design, and that after optimization. The motor before permeance design is named Motor A, the motor that has not been optimized after permeance design is named Motor B, and the motor after optimization is named Motor C.

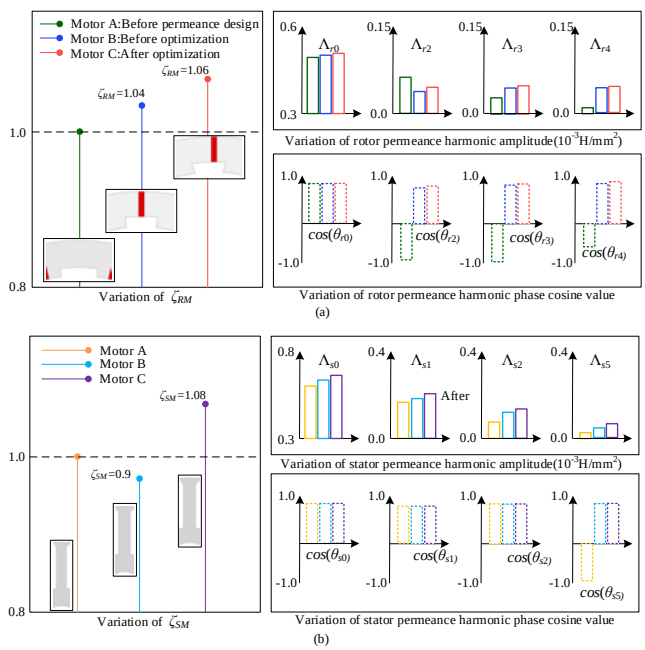


Fig. 14. Comprehensive evaluation of airgap permeance harmonics and lightweight characteristics. (a) Rotor side. (b) Stator side.

*1) Airgap permeance harmonics and light-weighting characteristics*

Fig. 14(a) reveals enhanced amplitude in the positive-torque-contributing 0th harmonic for the modulated design, improving torque capability. Crucially, harmonics previously generating negative torque components, namely 2nd, 3rd, and 4th rotor permeance harmonics, are transitioned to positive contributions, further augmenting torque output. The rotor light-weighting factor increases due to permeance modifications, satisfying mass reduction objectives. After optimization, this factor exhibited further improvement alongside amplified amplitudes of positive-torque harmonics. Analogous result in stator side is shown in Fig. 14(b), the light-weighting factor increased from 1 to 1.08. The amplitudes of 0th, 1st, and 2nd harmonics generating positive torque are enhanced, while formerly negative-contributing harmonics convert to positive torque generation. These results confirm partial achievement of the light-weighting design targets.

*2) Airgap flux density harmonics and high-torque-density characteristics*

Fig. 15 demonstrates the significant contribution of flux density harmonics to torque density enhancement. Increments of the 7th and 19th torque-related harmonics elevate their respective average torque density contributions. After permeance design and optimization, the torque density of the 7th harmonic increases by 24.6% and 37.2%, while the 19th harmonic contribution rises by 64.6% and 23.6%. These improvements validate both the optimization efficacy and the pivotal role of these harmonics in torque generation. Notably, torque density enhancement stems from both elevated torque output and reduced rotor volume, collectively confirming achievement of high-torque-density and lightweight design objectives.

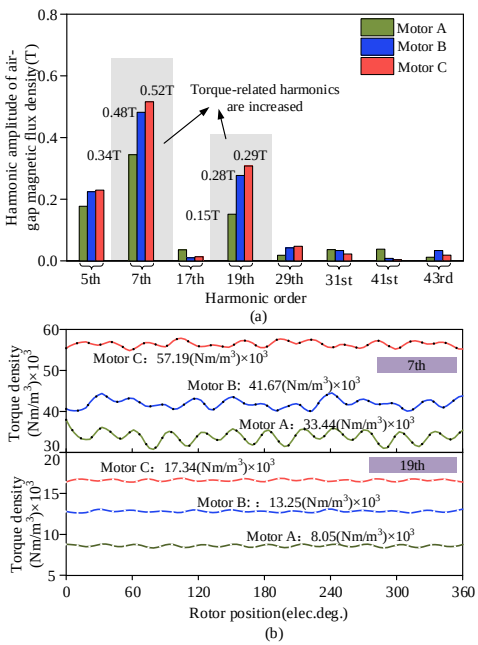


Fig. 15. Characteristic analysis of permeance-harmonic-oriented design and flux-density-harmonic-oriented optimization effect. (a) Airgap harmonics. (b) Torque density.

Fig. 16(a) presents the comparison results of torque performance. After the permeance harmonic design, the output torque of Motor B is 18.3 N·m, with a torque ripple of 16.5%. After optimization, compared with Motor A, the average torque of Motor C has increased by 6.2 N·m, and the torque ripple has decreased by approximately 47%. The torque performance of the motor has been effectively improved, which can prove the effectiveness of the design and optimization. Meanwhile, due to the improvement of the output power, the efficiency of the FMPMH motor is increased, as shown in Fig. 16(b). The efficiency of Motor C is 79.8%, which is higher than that of Motor A and Motor B.

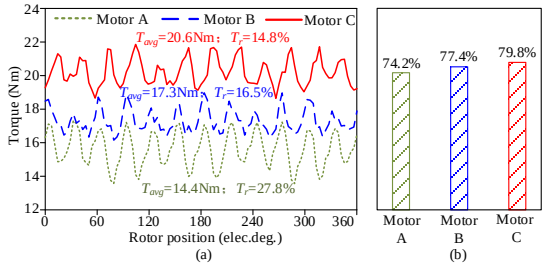


Fig. 16. Performance comparison of the three motors. (a) Torque. (b) Efficiency.

## V. Experimental Verification

To verify the foregoing analyses, a prototyped motor after permeance-harmonic-oriented design and optimization is manufactured and tested. Fig. 17(a) presents the prototype, and the basic parameters are listed in Table V. The experimental platform is shown in Fig. 17(b), including the tested prototype, torque speed sensor, magnetic powder brake, and so on.

TABLE V
BASIC PARAMETERS OF THE PROTOTYPE

| Item | Value | Items | Value |
|---|---|---|---|
| Outer radius of the rotor/mm | 87 | Rotor slot outer width, $\beta_{rso}$/° | 12.7 |
| Outer radius of the stator/mm | 69.3 | Stator pole arc width, $\beta_{so}$/° | 13.5 |
| Inner radius of the stator/ mm | 18 | Stator tooth angle, $\beta_{st}$/° | 18 |
| Airgap length/mm | 0.7 | Rotor slot height, $h_{rs}$/mm | 4.8 |
| Stack length/mm | 50 | Rotor slot inner width, $\beta_{rsi}$/° | 11.1 |
| PM pole arc angle, $\beta_{pm}$/° | 2.2 | Slot position angle, $\alpha$/° | 15 |

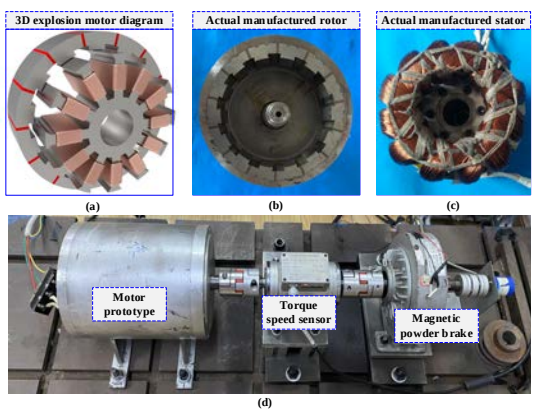


Fig. 17. Prototype and experimental platform of the investigated FMPMH motor. (a) 3D explosion motor diagram. (b) Actual manufactured rotor. (c) Actual manufactured stator. (d) Test platform.

The steady-state torque of the prototype is experimentally determined and analyzed. The motor operates under vector control, with a given speed of 300 r/min and a load of 16 N·m, featuring “high torque at low speed”. The measured torque waveform is shown in Fig. 18. As can be seen from Fig. 18, the motor can always maintain a stable output torque at 300 r/min.

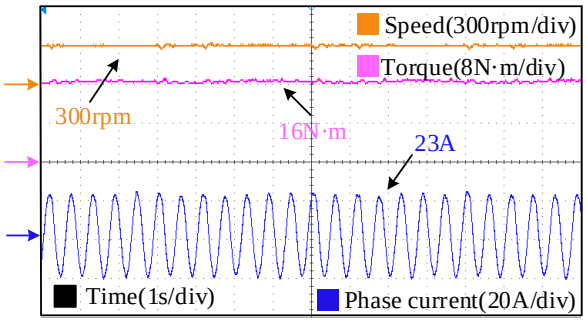


Fig. 18. Experimental waveform of steady load.

Fig. 19 shows the experimental results of motor torque characteristics under different speeds. Performance tests are carried out under conditions of 75, 150, 300, and 600 r/min. The prototype motor can operate stably under multiple speeds and achieve relatively ideal torque characteristics.

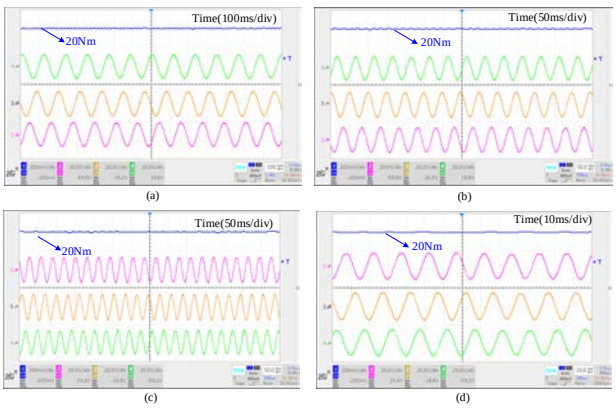


Fig. 19. The waveforms of the torque and current under different speeds. (a) 75 r/min. (b) 150 r/min. (c) 300 r/min. (d) 600 r/min.

In addition to steady-state characteristics, response speed is also a key performance of hub motors, which is related to the sensitivity of distributed drive EVs when passing through obstacle sections or encountering unexpected situations. Based on this, the dynamic response speed of the motor is also measured as shown in Fig. 20, mainly including the constant-speed variable-load response characteristic, and the constant-load variable-speed response characteristic.

Fig. 20(a) presents the response characteristics of the motor under constant speed and variable load. The motor starts at a constant no-load speed of 300 r/min and is loaded at 8 N·m every 4 s. When the motor is loaded, its rotational speed remains basically unchanged, while the current amplitude increases rapidly. Especially when the motor load increases from 8 to 16 N·m, the amplitude of the phase current rapidly doubles, while the motor speed remains stable. In addition, Fig. 20(b) shows the variable-speed response process of the motor from startup to 200 r/min, increasing to 400 r/min, and then to 600 r/min. During the acceleration process, both the current and torque increase, and the overdrive is relatively small. This also indirectly demonstrates the fast response speed characteristic of the motor.

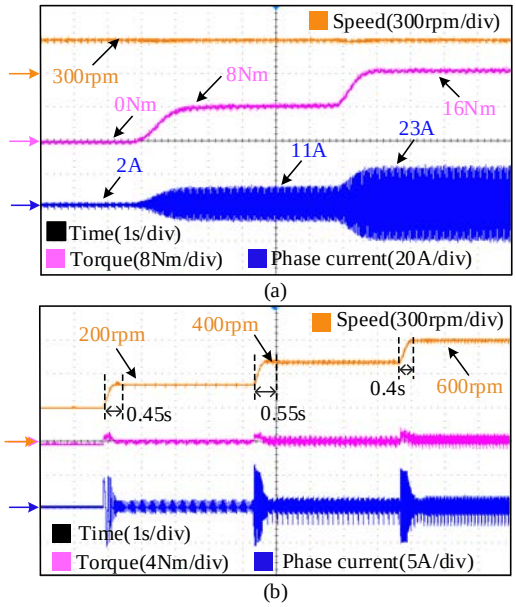


Fig. 20. Variable load and variable speed response test waveform of FMPMH motor. (a) Response characteristics under constant speed and variable load. (b) Response characteristics under constant load and variable speed.

## VI. Conclusion

In this paper, a method from the perspective of permeance-harmonic-oriented design and optimization is proposed and investigated, which is applied to FMPMH motors to improve torque quality and reduce the motor weight. The conclusions obtained during the research process are summarized as follows:

1) The internal relationship between the rotor and stator permeance harmonics and motor torque is established, and the torque contribution factor of airgap permeance harmonic is defined. Based on this, the key permeance harmonics are screened.

2) The selection criteria of the stator and rotor topology are established, and the amplitude and phase characteristics of the permeance harmonic group are considered in the process, which reflects the aggregation of the key permeance harmonics.

3) Taking the high output torque and lightweight of the motor as the design requirements, based on the generation mechanism of airgap flux density harmonics, a multi-objective aggregated optimization strategy is proposed. Sensitivity analysis and response surface analysis are used to narrow the selection range, reduce the motor optimization dimension, and improve the optimization efficiency to a certain extent.

Through design and optimization above, the motor achieves high torque density and low-speed high-torque characteristics, which have the application potential of a hub motor. Further discussions about extending and applying this approach to

other performance, such as power factor and efficiency, will be future research.

## APPENDIX

According to the principle of magnetic field modulation, the airgap harmonic modulation process in PM magnetic field and armature magnetic field can be decoupled. The modulation function of rotor and stator can be expressed as (A1) and (A2):

$$\Lambda_{\mathrm{r}}(\theta,t)=\Lambda_{\mathrm{r},0}-\sum_{n=1}\Lambda_{rn}\cos\left(nN_{\mathrm{r}}\theta-nN_{\mathrm{r}}\omega_{\mathrm{r}}t\right) \tag{A1}$$

$$\Lambda_{\mathrm{s}}(\theta)=\Lambda_{\mathrm{s},0}-\sum_{v=1}\Lambda_{sv}\cos\left(vN_{\mathrm{s}}\theta+\beta_v\right) \tag{A2}$$

where $\Lambda_{\mathrm{r}0}$ and $\Lambda_{\mathrm{s}0}$ are the coefficients of the zero-order of rotor and stator. And, $\Lambda_{rn}$ and $\Lambda_{sv}$ are those of permeance harmonic component. $n$ and $v$ denote positive integers, $N_{\mathrm{r}}$ and $N_{\mathrm{s}}$ are the number of rotor and stator modulation teeth. $\omega_{\mathrm{r}}$ is the mechanical angular speed of rotor.

Due to the modulating action of rotor and stator, the airgap flux density of PM and armature magnetic field can be calculated respectively as (A3) and (A4):

$$\begin{aligned}
&B_{\mathrm{pm_r_s}}(\theta,t)=\frac{\mu_0}{g}F_{\mathrm{pm}}(\theta,t)\cdot\Lambda_{\mathrm{r}}(\theta,t)\cdot\Lambda_{\mathrm{s}}(\theta)\\
&=F_{\mathrm{pm1}}\Lambda_{\mathrm{r}0}\Lambda_{\mathrm{s}0}\sin\left(p_{\mathrm{r}}\theta-p_{\mathrm{r}}\omega_{\mathrm{r}}t\right)\\
&-\frac{1}{2}\sum_{v}F_{\mathrm{pm1}}\Lambda_{\mathrm{r}0}\Lambda_{sv}\sin\left[\left(p_{\mathrm{r}}\pm vN_{\mathrm{s}}\right)\theta-p_{\mathrm{r}}\omega_{\mathrm{r}}t\pm\beta_v\right]\\
&-\frac{1}{2}\sum_{n}F_{\mathrm{pm1}}\Lambda_{rn}\Lambda_{\mathrm{s}0}\sin\left[(1\pm2n)\,p_{\mathrm{r}}\left(\theta-\omega_{\mathrm{r}}t\right)\right]\\
&+\frac{1}{4}\sum_{n}\sum_{v}F_{\mathrm{pm1}}\Lambda_{rn}\Lambda_{sv}\sin\left[(1\pm2n)\,p_{\mathrm{r}}\left(\theta-\omega_{\mathrm{r}}t\right)\pm\left(vN_{\mathrm{s}}\theta+\beta_v\right)\right]
\end{aligned} \tag{A3}$$

$$\begin{aligned}
&B_{\mathrm{a_r_s}}(\theta,t)=\frac{\mu_0}{g}F_{\mathrm{a}}(\theta,t)\cdot M_{\mathrm{r}}(\theta,t)\cdot M_{\mathrm{s}}(\theta)\\
&=F_{\mathrm{a1}}\Lambda_{\mathrm{r}0}\Lambda_{\mathrm{s}0}\sin\left(p_{\mathrm{a}}\theta-p_{\mathrm{r}}\omega_{\mathrm{r}}t\right)\\
&-\frac{1}{2}\sum_{v}F_{\mathrm{a1}}\Lambda_{\mathrm{r}0}\Lambda_{sv}\sin\left[\left(p_{\mathrm{a}}\pm vN_{\mathrm{s}}\right)\theta-p_{\mathrm{r}}\omega_{\mathrm{r}}t\pm\beta_v\right]\\
&-\frac{1}{2}\sum_{n}F_{\mathrm{a1}}\Lambda_{rn}\Lambda_{\mathrm{s}0}\sin\left[\left(p_{\mathrm{a}}\pm nN_{\mathrm{r}}\right)\theta-(1\pm2n)\,p_{\mathrm{r}}\omega_{\mathrm{r}}t\right]\\
&+\frac{1}{4}\sum_{n}\sum_{v}F_{\mathrm{a1}}\Lambda_{rn}\Lambda_{sv}\sin\left[\left(p_{\mathrm{a}}\pm nN_{\mathrm{r}}\pm vN_{\mathrm{s}}\right)\theta-(1\pm2n)\,p_{\mathrm{r}}\omega_{\mathrm{r}}t\pm\beta_v\right]
\end{aligned} \tag{A4}$$

where $\mu_0$ is the vacuum permeability, $g$ is the airgap length. Besides, $F_{\mathrm{pm1}}$ and $F_{\mathrm{a1}}$ are the amplitudes of PM and armature MMF, respectively. $p_{\mathrm{r}}$ and $p_{\mathrm{a}}$ are the pole pairs of PM and armature field, separately.

TABLE AI
MAIN COMPONENT ANALYSIS OF AIRGAP HARMONIC FROM PM AND ARMATURE MAGNETIC FIELD

| Harmonic orders | PM field | Armature field |
|---|---|---|
| $\{p_{\mathrm{r}}\}/\{-p_{\mathrm{a}}+N_{\mathrm{s}}\}$ | $F_{\mathrm{pm1}}\Lambda_{\mathrm{s}0}\Lambda_{\mathrm{r}0}$ | $0.5F_{\mathrm{a1}}\Lambda_{\mathrm{s}1}\Lambda_{\mathrm{r}0}$ |
| $\{p_{\mathrm{r}}-N_{\mathrm{s}}\}/\{p_{\mathrm{a}}\}$ | $0.5F_{\mathrm{pm1}}\Lambda_{\mathrm{s}1}\Lambda_{\mathrm{r}0}$ | $F_{\mathrm{a1}}\Lambda_{\mathrm{s}0}\Lambda_{\mathrm{r}0}$ |
| $\{p_r\pm vN_{\mathrm{s}}\}/\{p_{\mathrm{a}}-(1\pm v)N_{\mathrm{s}}\}$ | $0.5F_{\mathrm{pm1}}\Lambda_{sv}\Lambda_{\mathrm{r}0}$ | $0.5F_{\mathrm{a1}}\Lambda_{\mathrm{s}\lvert1\pm v\rvert}\Lambda_{\mathrm{r}0}$ |
| $\{(1\pm2n)p_{\mathrm{r}}\}/\{-p_{\mathrm{a}}+N_{\mathrm{s}}\pm2np_{\mathrm{r}}\}$ | $0.5F_{\mathrm{pm1}}\Lambda_{\mathrm{s}0}\Lambda_{rn}$ | $0.25F_{\mathrm{a1}}\Lambda_{\mathrm{s}1}\Lambda_{rn}$ |
| $\{(1\pm2n)p_{\mathrm{r}}-N_{\mathrm{s}}\}/\{-p_{\mathrm{a}}\pm2np_{\mathrm{r}}\}$ | $0.25F_{\mathrm{pm1}}\Lambda_{\mathrm{s}1}\Lambda_{rn}$ | $0.5F_{\mathrm{a1}}\Lambda_{\mathrm{s}0}\Lambda_{rn}$ |
| $\{(1\pm2n)p_{\mathrm{r}}\pm vN_{\mathrm{s}}\}/\{-p_{\mathrm{a}}+(1\pm v)N_{\mathrm{s}}\pm2np_{\mathrm{r}}\}$ | $0.25F_{\mathrm{pm1}}\Lambda_{sv}\Lambda_{rn}$ | $0.25F_{\mathrm{a1}}\Lambda_{\mathrm{s}\lvert1\pm v\rvert}\Lambda_{rn}$ |

Based on this, the components of airgap harmonics in PM and armature magnetic field can be expressed in Table AI according to the reduced modulation process. And the airgap flux density could be obtained as:

$$B_{\mathrm{g}}(\theta,t)=B_{\mathrm{pm\_r\_s}}(\theta,t)+B_{\mathrm{a\_r\_s}}(\theta,t) \tag{A5}$$

The airgap flux density contains the PM and armature magnetic field component. The airgap harmonics of different orders are closely related to MMF and different permeance harmonics. Then the airgap harmonics associated with zero-order rotor permeance $\Lambda_{\mathrm{r}0}$, zero-order stator permeance $\Lambda_{\mathrm{s}0}$, and 1st-order stator permeance $\Lambda_{\mathrm{s}1}$ are listed in Table AII, that is airgap flux density harmonic with $P_{\mathrm{r}}$ and $P_{\mathrm{r}}+N_{\mathrm{s}}$.

TABLE AII
HARMONIC COMPONENT ANALYSIS OF AIRGAP HARMONIC ASSOCIATED WITH MAIN PERMEANCE HARMONICS

| Harmonic orders | PM field | Armature field |
|---|---|---|
| $P_{\mathrm{r}}-N_{\mathrm{s}}$ | $0.5F_{\mathrm{pm1}}\Lambda_{\mathrm{s}1}\Lambda_{\mathrm{r}0}$ | $F_{\mathrm{a1}}\Lambda_{\mathrm{s}0}\Lambda_{\mathrm{r}0}$ |
| | $0.25F_{\mathrm{pm1}}\Lambda_{\mathrm{S}1}\Lambda_{\mathrm{R}1}$ | $0.5F_{\mathrm{a1}}\Lambda_{\mathrm{s}0}\Lambda_{\mathrm{r}1}$ |
| $P_{\mathrm{r}}$ | $F_{\mathrm{pm1}}\Lambda_{\mathrm{s}0}\Lambda_{\mathrm{r}0}$ | $0.5F_{\mathrm{a1}}\Lambda_{\mathrm{s}1}\Lambda_{\mathrm{r}0}$ |
| | $0.5F_{\mathrm{pm1}}\Lambda_{\mathrm{s}0}\Lambda_{\mathrm{R}1}$ | $0.25F_{\mathrm{a1}}\Lambda_{\mathrm{S}1}\Lambda_{\mathrm{r}1}$ |
| $P_{\mathrm{r}}+N_{\mathrm{s}}$ | $0.5F_{\mathrm{pm1}}\Lambda_{\mathrm{s}1}\Lambda_{\mathrm{r}0}$ | $0.5F_{\mathrm{a1}}\Lambda_{\mathrm{s}2}\Lambda_{\mathrm{r}0}$ |
| | $0.25F_{\mathrm{pm1}}\Lambda_{\mathrm{S}1}\Lambda_{\mathrm{R}1}$ | $0.5F_{\mathrm{a1}}\Lambda_{\mathrm{s}0}\Lambda_{\mathrm{r}1}$ |

## REFERENCES


[1] X. Y. Zhu, M. Jiang, and Z. X. Xiang *et al*., "Design and Optimization of a Flux-modulated Permanent Magnet Motor based on an Airgap-harmonic-orientated Design Methodology," *IEEE Trans. on Ind. Electron.*, vol. 67, no. 7, pp. 5337-5348, Jul. 2020.

[2] K. Toker, O. Tosun, and N. F. O. Serteller *et al*., "Design, Optimization and Experimental Study of Axial and Hub BLDC Motors In-wheel Application for Light Electric Vehicles," in *Proc. of 2022 IEEE 21st Mediterranean Electrotechnical Conference (MELECON)*, Palermo, Italy, Jun. 2022, pp. 354-359.

[3] L. Zhang, X. Q. Li, and X. Y. Zhu *et al*., "Design and Optimization of a Five-phase Reverse-salient Fault-tolerant Permanent Magnet Motor for Electric Vehicles," *IEEE Trans. on Ind. Electron*., vol. 72, no. 7, pp. 6762-6774, Jul. 2025.

[4] L. Zhang, Y. H. Wu, and X. Y. Zhu *et al*., "Autonomous Sensorless Control Strategy for FP-PMSM Considering Operation Uncertainties with DCEE," *IEEE Trans. on Transp. Electrif.*, pp. 1-1, Feb. 2026.

[5] Y. Li, S. C. Ding, and J. Hang *et al*., "A New Perspective on High-torque-density Mechanism of Permanent Magnet Vernier Machines," *IEEE Trans. on Energy Convers.*, vol. 39, no. 4, pp. 2337-2348, Dec. 2024.

[6] Y. L. Yu, F. Chai, and Y. L. Pei *et al*., "Investigation of Power Factor Characteristic in Permanent Magnet Motors for In-wheel Direct Drive Application," *IEEE Trans. on Energy Convers.*, vol. 39, no. 3, pp. 1699-1710, Sept. 2024.

[7] H. Hua, H. R. Ge, and Z. Q. Zhu *et al*., "Torque Improvement and Magnet Reduction of Flux Reversal Permanent Magnet Machines," *IEEE Trans. on Energy Convers.*, vol. 40, no. 3, pp. 1798-1809, Sept. 2025.

[8] J. R. Zhou, D. Y. Fan, and Z. X. Xiang *et al*., "Production Mechanism of Power Factor of V-type Vernier Permanent Magnet Machine and Improvement Method," *Trans. on China Electrotech. Soc.*, vol. 38, no. 14, pp. 3789-3799, Jul. 2023.

[9] Y. L. Yu, Y. L. Pei, and F. Chai *et al*., "Performance Comparison Between Permanent Magnet Synchronous Motor and Vernier Motor for In-wheel Direct Drive," *IEEE Trans. on Ind. Electron*., vol. 70, no. 8, pp. 7761-7772, Aug. 2023.

[10] X. L. Li, Z. Wei, and Y. J. Zhao *et al*., "Design and Analysis of Surface-mounted Permanent-magnet Field-modulation Machine for Achieving High Power Factor," *IEEE Trans. on Ind. Electron.*, vol. 71, no. 5, pp. 4375-4386, May 2024.

[11] X. K. Zhu, D. J. Zhao, and M. Cheng *et al*., "Mathematical Model and Vector Control of SPMSM Considering Eddy Current and Hysteresis Effects based on Vector Magnetic Circuit Theory," *IEEE Trans. on Power Electron.*, vol. 41, no. 5, pp. 7383-7393, May 2026.

[12] X. L. Li, Y. C. Tian, and W. B. Dai *et al*., "Three-phase Decoupling SVPWM-based Natural Fault-tolerant Control of Six-phase Vernier PM Motor with Open-phase Fault for Reducing Torque Ripple," *IEEE J. of Emerg. and Sel. Topics in Power Electron.*, vol. 14, no. 1, pp. 411-421, Feb. 2026.

[13] X. K. Zhu, Y. B. Liu, and M. M. Li *et al*., "Design, Analysis and Test of the Dual Three-phase Permanent Magnet Vernier Superconducting Armature Electrical Machine Prototype," *Supercond. Sci. and Technol*., vol. 38, no. 12, pp. 125031, Dec. 2025.

[14] H. Chen, D. W. Li, and Y. Meng *et al*., "Investigation of a Novel Dual-side PM Vernier Machine with Two-slot-pitch Coils," *IEEE Trans. on Transp. Electrif*., vol. 11, no. 1, pp. 2108-2119, Feb. 2025.

[15] W. X. Zhao, Q. Z. Hu, and J. H. Ji *et al*., "Torque Generation Mechanism of Dual-permanent-magnet-excited Vernier Machine by Air-gap Field Modulation Theory," *IEEE Trans. on Ind. Electron*., vol. 70, no. 10, pp. 9799-9810, Oct. 2023.

[16] C. S. Liu, Y. X. Xu, and J. B. Zou *et al*., "Permanent Magnet Shape Optimization Method for PMSM Air Gap Flux Density Harmonics Reduction," *CES Trans. on Electr. Mach. and Syst*., vol. 5, no. 4, pp. 284-290, Dec. 2021.

[17] Z. X. Li, J. K. Xia, and T. F. Liu *et al*., "Reduction of Local Tangential Force of Fractional-slot Concentrated Winding Permanent Magnet Synchronous Machines with Piecewise Stagger Trapezoidal Poles," *Trans. of China Electrotech. Soc*., vol. 38, no. 6, pp. 1447-1459, Mar. 2023.

[18] Y. T. Gao, J. Z. Li, and Y. Liu *et al*., "Analysis of a Vernier Machine with Buried Halbach-array Permanent Magnets," *IEEE Trans. on Transp. Electrif*., vol. 11, no. 1, pp. 4035-4046, Feb. 2025.

[19] Q. Chen, J. H. Liao, and W. Qian *et al*., "Design and Optimization a New Spoke-type Flux-modulation Machine with Inverted T-shape Permanent Magnets," *IEEE Trans. on Energy Convers.*, vol. 38, no. 1, pp. 203-217, Mar. 2023.

[20] X. K. Zhu, C. H. Song, and M. Cheng *et al*., "Coordinate Transformation based on Vector Magnetic Circuit Theory and Its Application in Sensorless Control of SPMSM," *IEEE Trans. on Ind. Electron.*, vol. 73, no. 5, pp. 6669-6679, May 2026.

[21] Z. X. Xiang, Y. T. Zhou, and X. Y. Zhu *et al*., "Research on Characteristic Airgap Harmonics of a Double-rotor Flux-modulated PM Motor based on Harmonic Dimensionality Reduction," *IEEE Trans. on Transp. Electrif*., vol. 10, no. 3, pp. 5750-5761, Sept. 2024.

[22] Y. H. Sun, W. X. Zhao, and J. H. Ji *et al*., "Overview of Multi-star Multi-phase Permanent Magnet Machines with High Torque Performance and Its Key Technologies," *Trans. of China Electrotech. Soc*., vol. 38, no. 6, pp. 1403-1420, Mar. 2023.

[23] R. Xu, and W. M. Tong, "Multi-objective Hierarchical Optimization of Interior Permanent Magnet Synchronous Machines based on Rotor Surface Modification," *CES Trans. on Electr. Mach. and Syst*., vol. 6, no. 4, pp. 352-358, Dec. 2022.

[24] Z. X. Xiang, J. Q. Wei, and X. Y. Zhu, "Torque Ripple Suppression of a PM Vernier Machine from Perspective of Time and Space Harmonic Magnetic Field," *IEEE Trans. on Ind. Electron.*, vol. 71, no. 9, pp. 10150-10161, Sept. 2024.

[25] B. Wang, R. X. Wang, and H. W. Cai *et al*., "Optimal Airgap Permeance Design for Magnetic Field Modulated Permanent Magnet Vernier Machine," *IEEE Trans. on Energy Convers.*, vol. 40, no. 4, pp. 2760-2769, Dec. 2025.

[26] T. Y. Zhou, L. W. Shi, and S. F. Shi *et al*., "Vibration Analysis and Optimization of E-type Modular Stator Permanent Magnet Motor Considering Teeth Modulation," *IEEE Trans. on Energy Convers.*, vol. 41, no. 1, pp. 734-747, Mar. 2026.

[27] Y. Z. Zheng, Z. Q. Zhu, and H. Xu *et al*., "Optimal Multi-tooth Numbers for Vernier PM Synchronous Machines," *IEEE Access*, vol. 12, pp. 89599-89612, Jun. 2024.

[28] S. S, Luo, Y. Zhao, and D. W. Li *et al*., "A Novel Flux Switching Permanent Magnet Machine based on Quantitative Stator Permeance Construction Approach," *IEEE Trans. on Ind. Appli.*, vol. 61, no. 5, pp. 6916-6927, Sept.-Oct. 2025.

[29] P. X. Wang, W. Hua, and G. Zhang *et al*., "Principle of Flux-switching Permanent Magnet Machine by Magnetic Field Modulation Theory Part I: Back-electromotive-force Generation," *IEEE Trans. on Ind. Electron.*, vol. 69, no. 3, pp. 2370-2379, Mar. 2022.

[30] P. X. Wang, W. Hua, and G. Zhang *et al*., "Principle of Flux-switching PM Machine by Magnetic Field Modulation Theory part II: Electromagnetic Torque Generation," *IEEE Trans. on Ind. Electron.*, vol. 69, no. 3, pp. 2437-2446, Mar. 2022.

[31] L. Fang, D. W. Li, and R. H. Qu, "Torque Improvement of Vernier Permanent Magnet Machine with Larger Rotor Pole Pairs than Stator Teeth Number," *IEEE Trans. on Ind. Electron.*, vol. 70, no. 12, pp. 12648-12659, Dec. 2023.

[32] H. Chen, D. W. Li, and R. H. Qu *et al*., "Torque Capacity Improvement of Flux-switching PM Machines based on Directional Stator Permeance Design," *IEEE Trans. on Ind. Electron.*, vol. 71, no. 5, pp. 4551-4561, May 2024.

[33] L. Fang, Y. Z. Zhang, and D. W. Li *et al*., "Synthesis of Consequent Pole Vernier Permanent Magnet Machine based on Oscillating Magnetic Potential Difference Model," *IEEE Trans. on Transp. Electrif*., vol. 10, no. 2, pp. 3231-3245, Jun. 2024.

[34] Z. J. Ling, Y. C. Yuan, and W. X. Zhao *et al*., "Permeance Reconfiguration in Flux Modulation Permanent Magnet Machines with Transcription Waveform Method," *IEEE Trans. on Energy Convers.*, pp. 1-10, Sept. 2025.

[35] J. W. Zhou, M. Cheng, and H. H. Wen *et al*., "Modeling and Suppression of Torque Ripple in PMSM based on the General Airgap Field Modulation Theory," *IEEE Trans. on Power Electron*., vol. 37, no. 10, pp. 12502-12512, Oct. 2022.

[36] B. D. Wang, D. H. Wang, and C. Peng *et al*., "Interior Permanent Magnet Synchronous Machines with Composed T-shaped Notching Rotor," *IEEE Trans. on Ind. Electron.*, vol. 71, no. 6, pp. 5519-5529, Jun. 2024.

[37] Z. Z. Ma, M. Cheng, and H. H. Wen, "Analysis and Optimization of Rotor Salient Pole Reluctance Considering Multi-modulation Orders," *IEEE Trans. on Ind. Electron*., vol. 70, no. 11, pp. 10871-10880, Nov. 2023.

**Yuting Zhou** (Student member, IEEE) received the B.Sc. degree in electrical engineering from Jiangsu University, Zhenjiang, China, in 2021, where she is currently working towards the Ph.D. degree in electrical engineering.

Her current research interests include the design and analysis of flux-modulated permanent magnet machines for electric vehicles.

**Zixuan Xiang** (Member, IEEE) received the B.Sc. degree from Hubei Polytechnic University, Huangshi, China, in 2010, the M.Sc. and the Ph.D. degrees in power electronics and power transmission from the School of Electrical and Information Engineering, Jiangsu University, Zhenjiang, China, in 2017.

He is currently an associate professor in School of Electrical and Information Engineering, Jiangsu University. His main research interests include design, optimization, and drive control of high-performance permanent magnet motor and novel double mechanical port permanent magnet motor for application in modern electric vehicles and hybrid electric vehicles.

**Xiaoyong Zhu** (M'09) received the B.Sc. and M.Sc. degrees in electrical engineering from Jiangsu University, Zhenjiang, China, in 1997 and 2002, respectively, and the Ph. D degree from the School of Electrical Engineering, Southeast University, Nanjing, China, in 2008.

He has been with Jiangsu University since 1999, where he is currently a Professor with the School of Electrical Information Engineering. In 2007-2008, he was a Research Assistant with the Department of Electrical and Electronic Engineering, University of Hong Kong. From 2012 to 2013, he was a Visiting Professor with the Department of Energy-Funded Graduate Automotive Technology Education Center for Electric Drive Transportation, University of Michigan, Dearborn, Michigan, USA. His current research interests include design and drive control of electric machines with wide-speed range, less rare-earth permanent magnet motor, and multi-port permanent magnet motor. In these areas, he has authored and co-authored more than 70 referred technical papers, and holds 12 patents.

**Qian Liu** received the B.Sc. degree in Physics from Hubei University, Wuhan, China, in 2010, the M.Sc. degree in Education from the School of Teacher Education, Jiangsu University, Zhenjiang, China, in 2017.

She is currently an experimentalist in School of Physics and Electronic Engineering, Jiangsu University. Her main research interests include electromagnetic field analysis and computation

**Deyang Fan** (Member, IEEE) received the B.Sc. degree in electrical engineering from North China Electric Power University, Baoding, China, in 2014, and the Ph.D. degree in electrical engineering from Jiangsu University, Zhenjiang, China in 2021. From 2019 to 2020, he was with the Department of Electrical and Computer Engineering, University of Kentucky, Lexington, KY, USA, as a Joint Ph.D. Student.

He is currently a lecturer in School of Electrical and Information Engineering, Jiangsu University. His current research interests include modeling, design, optimization, and control of high-performance permanent magnet motors for electric vehicles.

**Kunhua Chen** received the B.Sc., M.Sc., and Ph.D. degrees in electrical engineering from Jiangsu University, Zhenjiang, China, in 2003, 2006, and 2016, respectively.

He is currently an associate professor in School of Electrical and Information Engineering, Jiangsu University. His main research interests include design, optimization, and drive control of permanent magnet motor for application in modern electric vehicles and hybrid electric vehicles.